Electronic Supplementary Material (ESI) for Nanoscale.
This journal is © The Royal Society of Chemistry 2024

Carrier modulation of one-dimensional $MAPb_xSr_{1-x}(I_yCl_{1-y})_3$ core-shell perovskite nanowires

Pengjie Fu,[a] Mengni Liu,[a] Guixian Ge,[a] Jianguo Wan,[b] Xiaodong Yang*,[a]

[a] College of Sciences, Shihezi University, Shihezi 832003, China.

[b] Department of Physics, Nanjing University, Nanjing 210093, China.

Corresponding Author
***Email:** yangxiaodong1209@hotmail.com (X. D. Yang)

Table.S1 Band-gaps calculated in this work by using various theory methods for bulk $MAPbI_3$.

	PBE	SOC	HSE	Experience
O-phase	1.69	0.78	1.73	1.64[1]
T-phase	1.69	0.80	1.75	1.60[2]

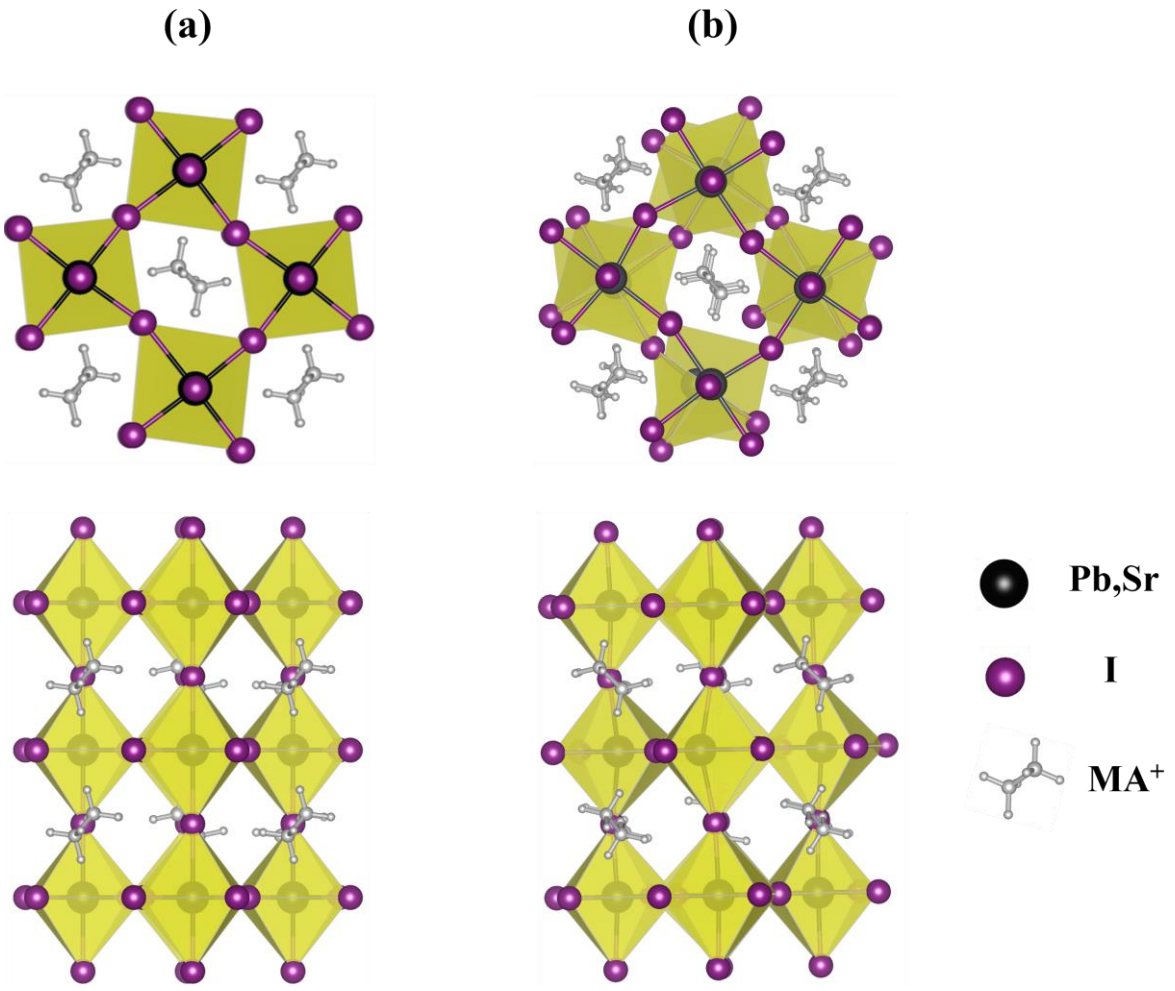

Fig.S1 Crystal structures of (a) orthorhombic (O-) and (b) tetragonal (T-) phases of $MAPbI_3$. The upper and lower panels represent [001] and [100] crystallographic directions, respectively.

Table.S2 Optimized lattice constants of $MAPbI_3$ and $MASrI_3$ in O-phase and T-phase.

lattice constant(Å)	**$MAPbI_3$**		**$MASrI_3$**	
	O-phase	T-phase	O-phase	T-phase
a	8.97(8.84[3],9.04[4])	8.80(8.85[3],8.83[5])	9.05(8.99[6])	8.87(8.79[7])
b	12.85(12.54[3],12.86[4])	--	12.96(13.00[6])	--
c	8.71(8.561,8.552)	12.89(12.641,12.982)	8.78(8.544)	13.01(12.92[7])

[1]Reference (3), experimental data
[2]Reference (4), DFT calculation data
[3]Reference (5), experimental data
[4]Reference (6), DFT calculation data
[5]Reference (7), DFT calculation data

In order to study perovskite nanowires, we first investigated the bulk structures of hybrid organic-inorganic halide perovskites. Here, we considered two common crystal phases **(Fig.S1)**, namely orthorhombic phase and tetragonal phase (labeled as O-phase and T-phase, respectively). **Fig.S1 a** and **Fig.S1 b** respectively shows the crystal structures of O-phase and T-phase $MAPbI_3$ ($MASrI_3$). The schematic diagrams above and below show the top and side views along the {010}, {001}, {100} and {001} crystal orientations of the O-phase (T-phase), respectively. Some previous studies[5,6] have also shown that Sr^{2+} has almost no effect on the crystal structure as a substitute element for Pb^{2+}. The reason why this element substitution can maintain the stability of the perovskite structure is because the radii of $Sr^{2+}$and $Pb^{2+}$are almost equal. The optimized lattice constants are shown in **Table.S2**, which listed the previous theoretical and experimental values for comparison. Although some studies have announced the synthesis of $MASrI_3$,[5-7] there is no experimental structural data and only theoretical calculation values are provided. Therefore, the data compared with $MASrI_3$ in **Table.S2** are all theoretical results. The lattice constant we calculated is consistent with previous theoretical and experimental data. The largest lattice mismatch occurs in the O-phase of $MASrI_3$ (less than 3%), which is caused by non-centrosymmetric $CH_3NH_3^+$

molecules and relatively relaxed organic-inorganic hybrid structures, indicating the reliability of our calculation results. The very close lattice constant between $MAPbI_3$ and $MASrI_3$ enables the composite system composed of $MAPbI_3$ and $MASrI_3$ to maintain its original perovskite structures well.

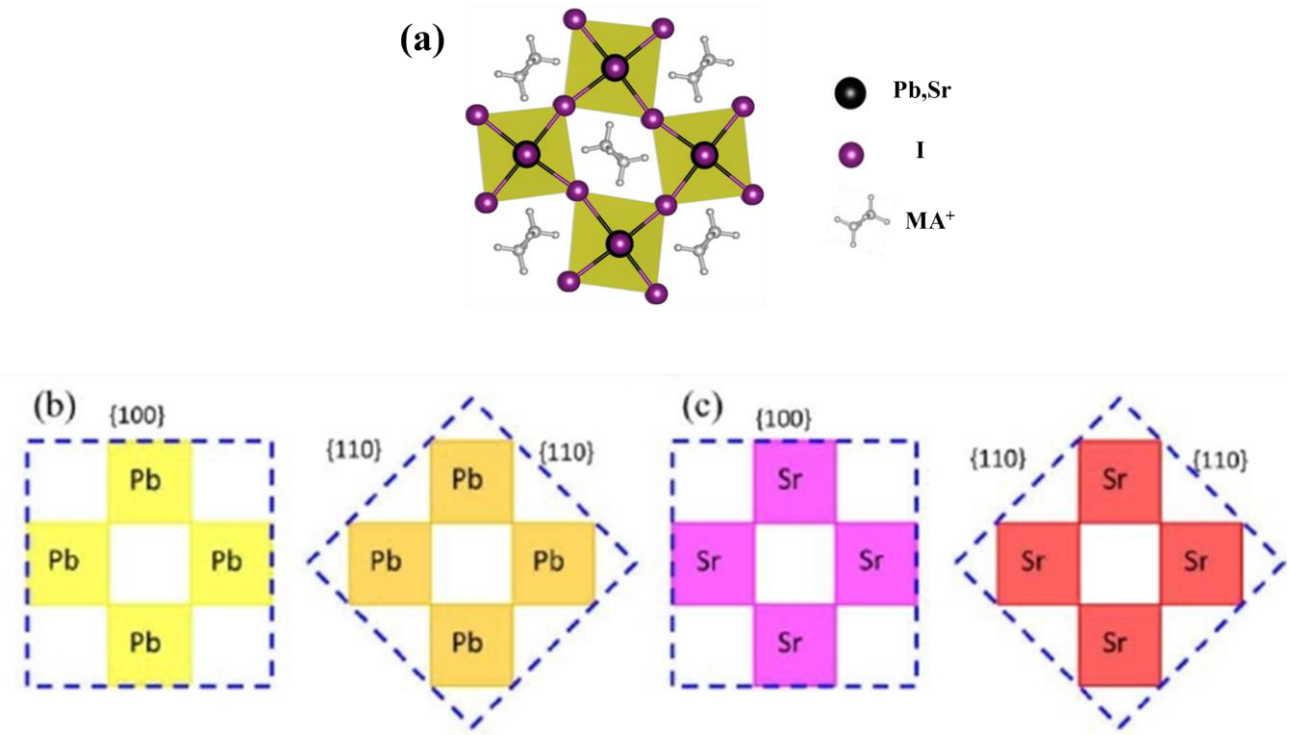

Fig.S2 Schematic diagrams of $MAPbI_3$ and $MASrI_3$ perovskite nanowires with {100} and {110} planes. The blue dashed line represents the surface of the nanowire.

On the basis of bulk perovskite, O-phase perovskite nanowires were constructed. We first discussed the structural stability of nanowires. In order to study the stability of nanowires, two types of nanowire surfaces were considered, as shown in **Fig.S2**, including {100} and {110} surfaces. **Fig.S2 b** shows schematic diagrams of rectangular cross-section perovskite nanowires surrounded by {100} and {110} of $MAPbI_3$ and $MASrI_3$, respectively. Due to the large surface/volume ratio of single crystal perovskite nanowires, the surface has significant impact on the stability of the nanowires. Therefore, by considering the surface energy of nanowires (γ_s) to study the stability of nanowires. We constructed surface structures of $MAPbI_3$ and $MASrI_3$(100)

and (110) crystal planes. As shown in **Fig.S3**, there are usually three types of surface terminals considered, namely flat, MAI and vacant terminals. They have already been studied similarly in T-phase $MAPbI_3$.[8] The surface of the vacant terminal has the same stoichiometric ratio as the perovskite phase, while the surfaces of the flat terminal and MAI terminal are composed of PbI_2 and MAI groups, respectively. Based on the surfaces of different terminal types mentioned above, the surface energy of each surface γ_s was calculated using the following formula:

$$\gamma_{vacant} = \frac{E_T - n_v E_{MAXI_2}}{2A} \quad \text{(S1)}$$

$$\gamma_s = \gamma_{vacant} + \frac{\Delta E_T - \Delta n_{MAI}\mu_{MAI} - \Delta n_{XI_2}\mu_{XI_2}}{2A} \quad \text{(S2)}$$

The surface energy of the vacant terminal surface was obtained from equation (S1), where E_T is the total energy of the vacant terminal surface, and E_{MAXI_2} is the average total energy per unit molecular formula in the orthogonal phase $MAXI_3$(X=Pb, Sr). A is the surface area, and n_v is the number of $MAXI_3$ units in the vacant terminal surface. Due to the special stoichiometric ratio of the surface of the vacant terminal, the surface energy γ_s of all terminals was calculated based on the surface energy of the vacant terminal surface. In equation (S2), ΔE_T is the total energy difference between the given surface and the vacant terminal surface. Due to the fact that $MAPbI_3$($MASrI_3$) nanowires are synthesized from MAI and PbI_2(SrI_2) as precursors,[9] we used the chemical potentials of the most stable reactants MAI and XI_2, namely μ_{MAI} and μ_{XI_2}, to describe extreme situations in different chemical environments. The allowable values of μ_{MAI} and μ_{XI_2} are limited by equation $\mu_{MAI} + \mu_{XI_2} = E_{MAXI_3}$, and the range of μ_{MAI} values is $E_{MAI(bulk)} - \Delta H_f \leq \mu_{MAI} \leq E_{MAI(bulk)}$. The upper (lower) limits of μ_{MAI} correspond to the chemical environment rich in MAI(XI_2), while ΔH_f

is the enthalpy of formation for orthorhombic perovskite blocks. The calculated O-phase $MAPbI_3$ and $MASrI_3$ blocks ΔH_f are 0.2673 eV and 0.2670 eV, respectively. $\Delta n_{MAI}(\Delta n_{XI_2})$ is the difference in the number of MAI(XI_2) between the given surface and the vacant terminal surface.

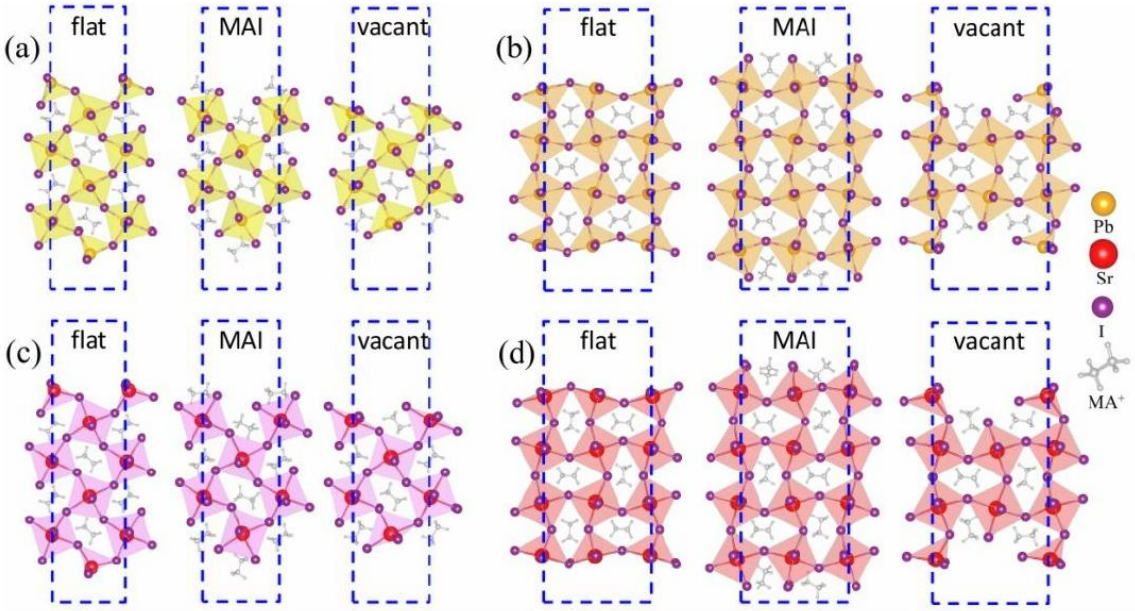

Fig.S3 Side views of the (a) {100} and (b) {110} surfaces of $MAPbI_3$ after optimization, as well as the (c) {100} and (d) {110} surfaces of $MASrI_3$. Each crystal plane has three terminal types: flat, MAI and vacant.

The surface energies of three types of terminals under different chemical environments is shown in **Fig.S4**. **Fig.S4 a** and **b** show the surface energies of $MAPbI_3$ {100} and {110} under conditions rich in MAI and PbI_2, respectively. The results indicate that the MAI terminal type of $MAPbI_3$ is the most stable surface, and its surface energy is significantly lower than other surface terminal types, whether under conditions rich in MAI and PbI_2 or between {100} and {100} surfaces. From an energy perspective, the flat and vacant terminal surfaces are relatively unstable. Similar to the case of $MAPbI_3$, as shown in **Fig.S4 c** and **d**, under conditions rich in MAI and PbI_2, the MAI terminal surface of $MASrI_3$ perovskite is the most stable surface type, while

other terminal types, including flat and vacant terminal surfaces remain less stable. The high stability of the MAI terminal structure surfaces of $MAPbI_3$ and $MASrI_3$ means that the surface of perovskite nanowires with MAI terminal surfaces is the most energetically favorable.

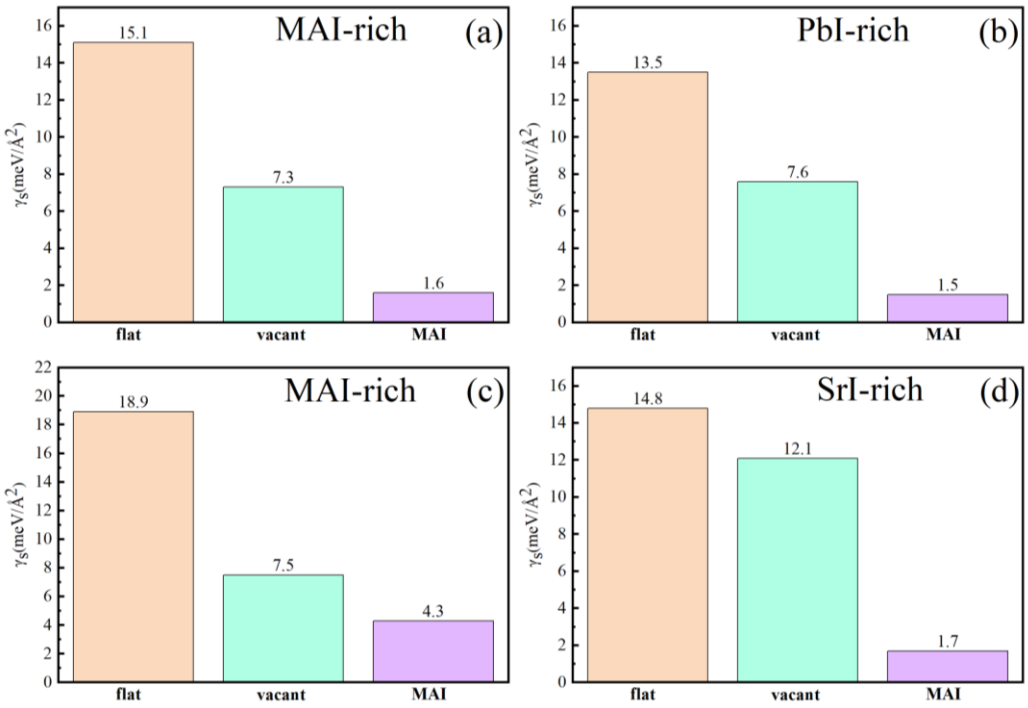

Fig.S4 The surface energies of the (a) {100} surface in MAI-rich chemical environment and (b) {110} surface in PbI_2-rich chemical environment of $MAPbI_3$. The surface energies of the (c) {100} surface in MAI-rich chemical environment and (d) {110} surface in SrI_2-rich chemical environment of $MASrI_3$.

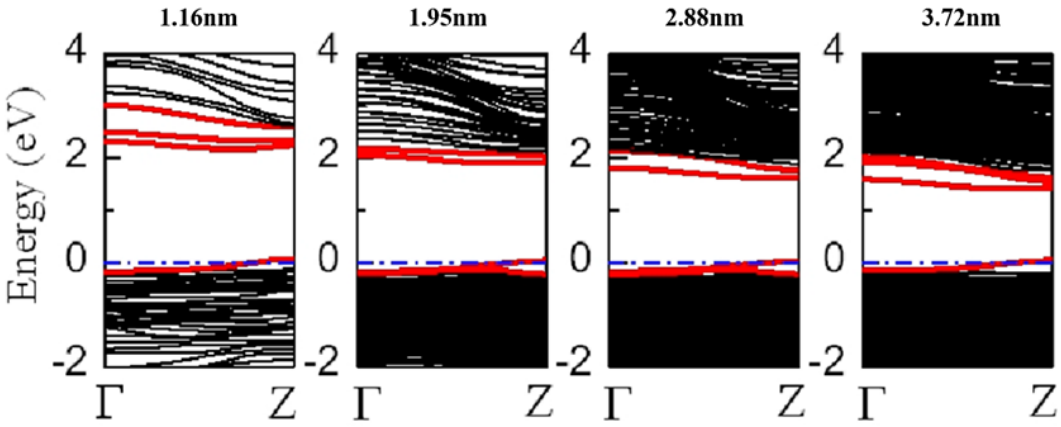

Fig.S5 Band structure diagrams of $MAPbI_3$ perovskite nanowires with {100} crystal planes at different sizes. The energy band marked in red represents the surface electronic state of the nanowires.

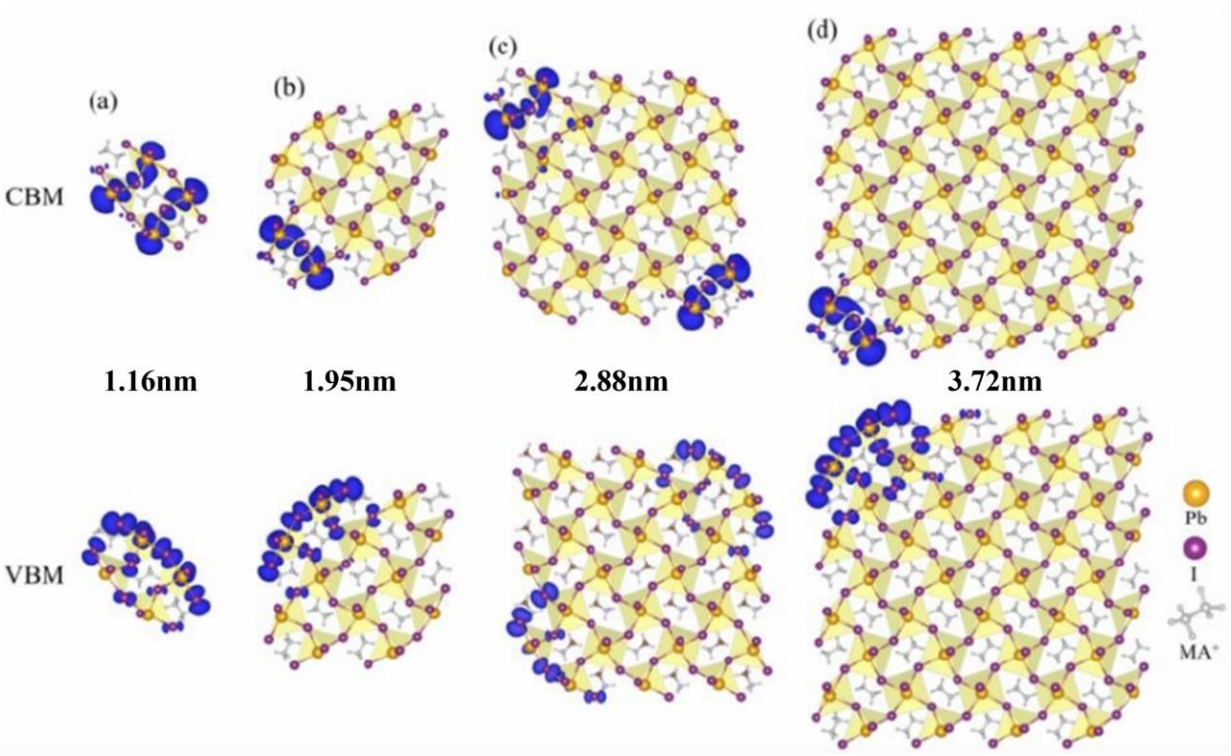

Fig.S6 The distribution of electronic states of the band edge of $MAPbI_3$ perovskite nanowires with {100} crystal planes at different sizes.

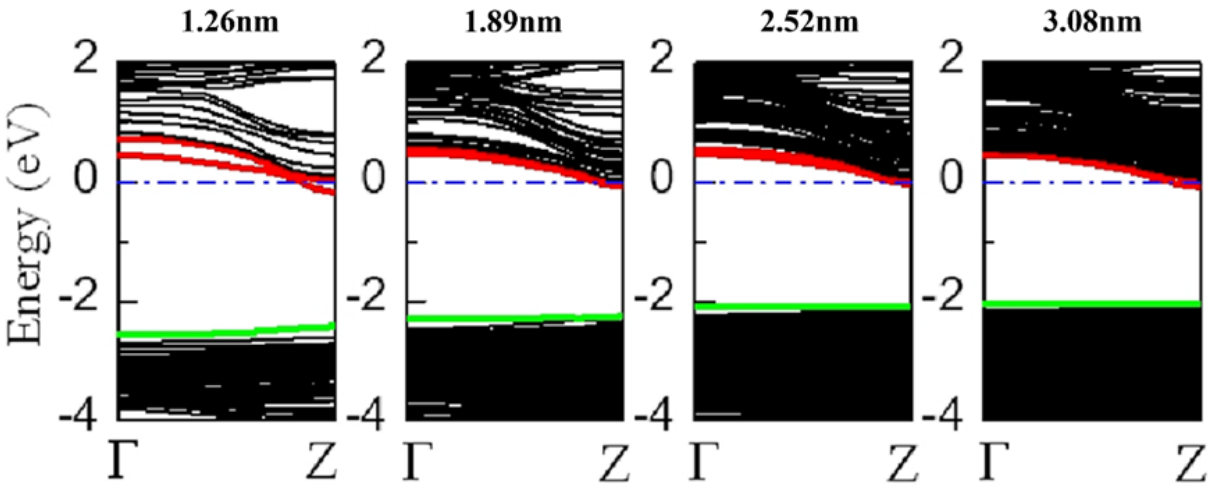

Fig.S7 Band structure diagrams of $MAPbI_3$ perovskite nanowires with {110} crystal planes at different sizes. The red band represents the surface electronic state of the nanowire, while the green band represents the first extended electronic state of the nanowires (including surface electronic state and bulk electronic state).

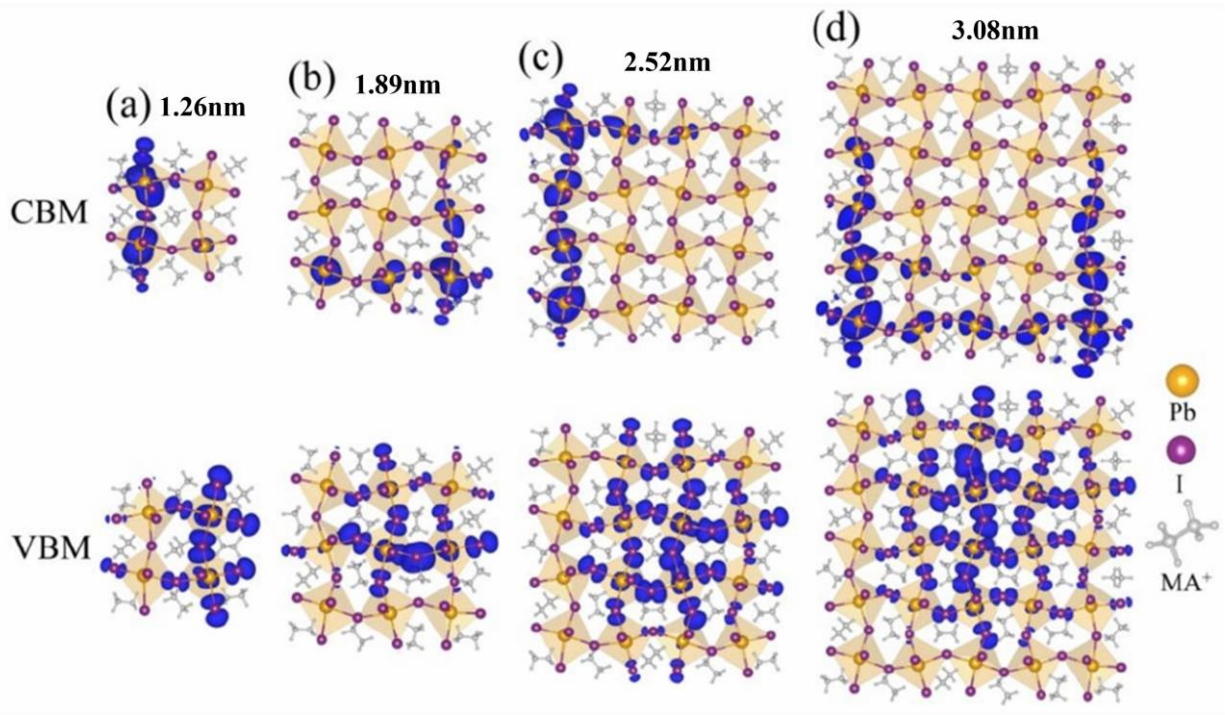

Fig.S8 The distribution of electronic states of the band edge of $MAPbI_3$ perovskite nanowires with {110} crystal planes at different sizes.

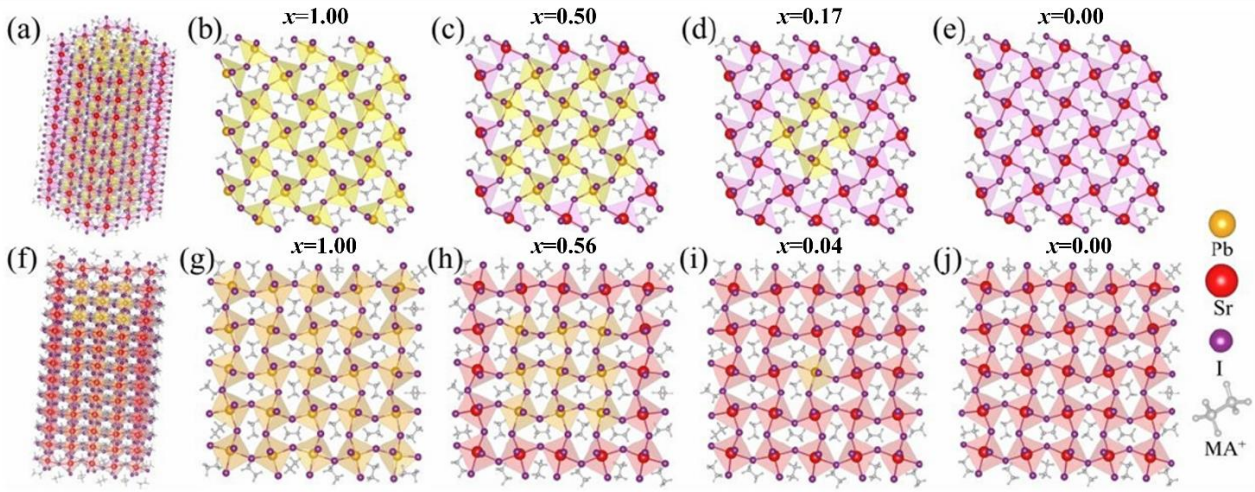

Fig.S9 Atomic structure diagrams of $MAPb_xSr_{1-x}I_3$ core-shell nanowires: (a) 3D structure of 2.88nm perovskite nanowires with {100} crystal planes, (b)-(e) cross-sectional views of nanowires with {100} crystal planes at different component x. (f) 3D structure of 3.08nm perovskite nanowires with {110} crystal planes, and (g)-(j) cross-sectional views of nanowires with {110} crystal planes at different component x.

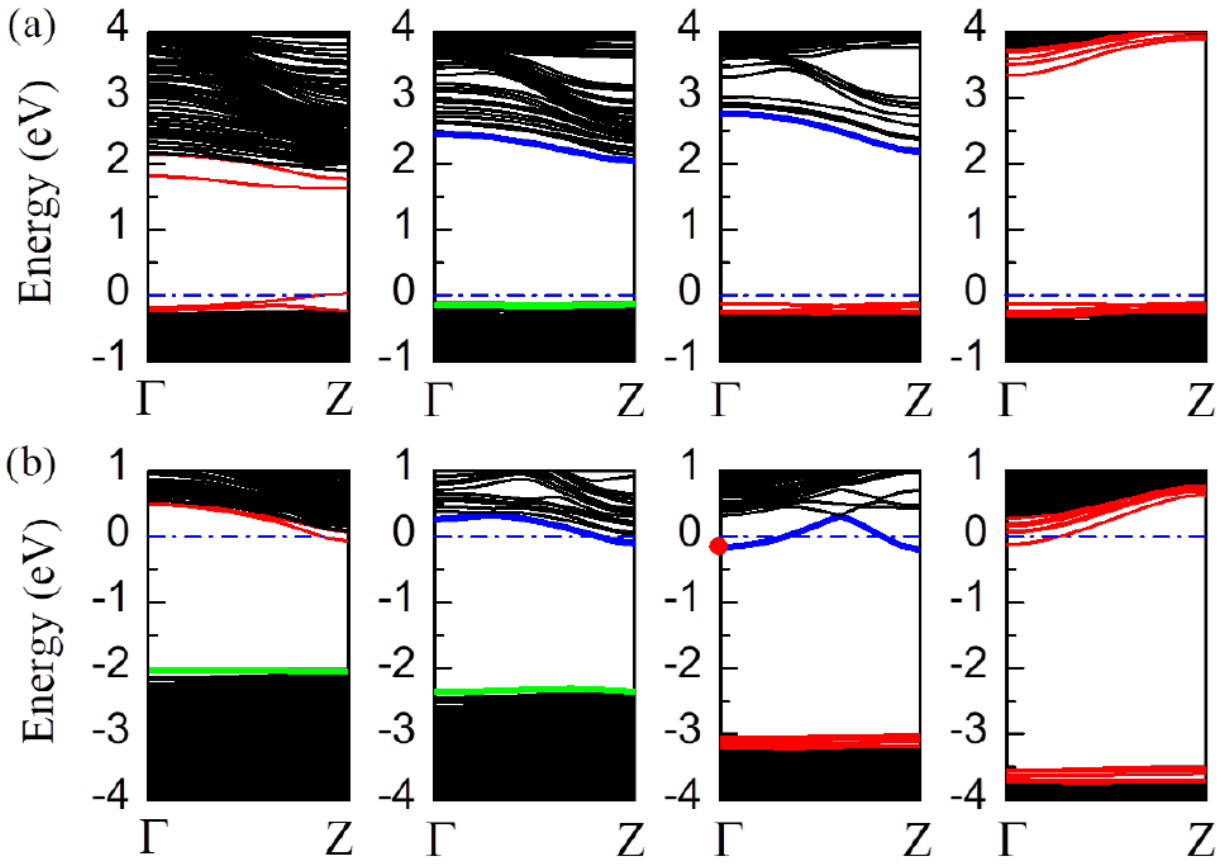

Fig.S10 (a) The energy band structures of $MAPb_xSr_{1-x}I_3$ core-shell nanowires with {100} crystal plane at different component *x*, (b) the energy band structures of {110} crystal plane nanowires at different component *x*.

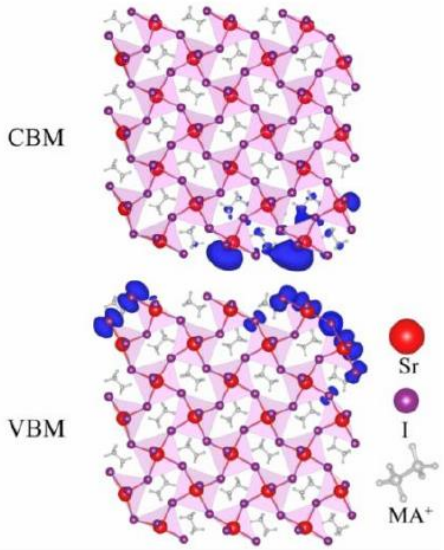

Fig.S11 Distribution of electronic states of the band edge in $MASrI_3$ perovskite nanowire with {100} crystal planes.

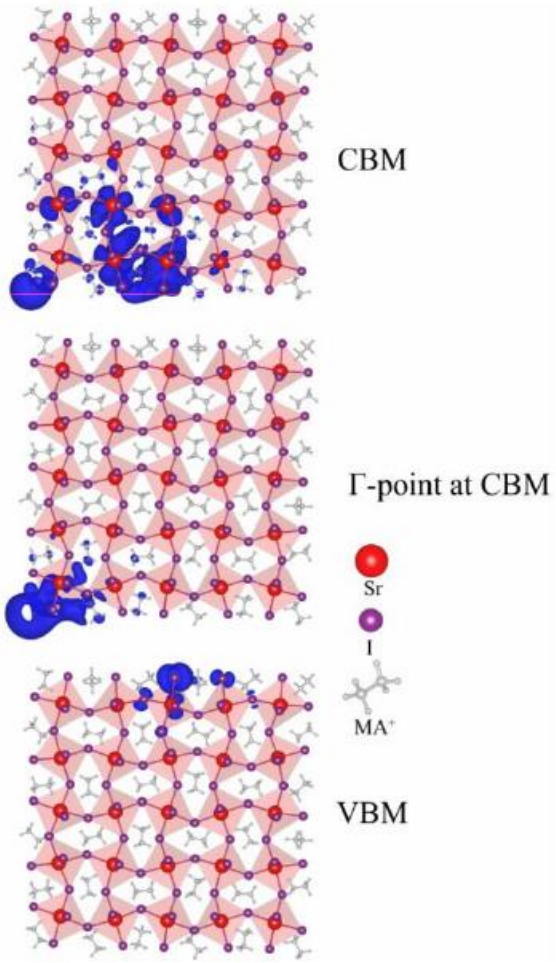

Fig.S12 Distribution of electronic states of the band edge in $MASrI_3$ perovskite nanowire with {110} crystal planes.

The component x decreases sequentially from **Fig.S9 b** to **e** and from **Fig.S9 g** to **j**. **Fig.S9 b**, **g** and **Fig.S9 e**, **j** respectively shows the two extreme structures of core-shell nanowires, namely the pristine $MAPbI_3$ and $MASrI_3$ nanowires. **Fig.S9 c** and **d** show the {100} crystal plane core-shell nanowires with components x=0.50 and 0.17, respectively. **Fig.S9 h** and **i** show the {110} crystal plane core-shell nanowires with components x=0.56 and 0.04, respectively. **Fig.S10 a** shows the band structure diagrams of {100} crystal plane core-shell nanowires with x=100%, 50%, 17%, and 0%, respectively, from left to right. **Fig.S10 b** shows the band structure diagrams of {110} crystal plane core-shell nanowires with x=100%, 56%, 4%, and 0%, respectively,

from left to right. The core-shell nanowires with x=0% are simply $MASrI_3$ nanowires, and their electronic state distributions of band edge are shown in **Fig.S11** and **Fig.S12**, it can be observed that similar to pristine $MAPbI_3$ nanowires, the electrons and holes at the band edge of pristine $MASrI_3$ nanowires are localized on their surface regardless of the crystal plane. These surface states promote the recombination of carriers, thereby reducing the diffusion length and lifetime of the carriers.

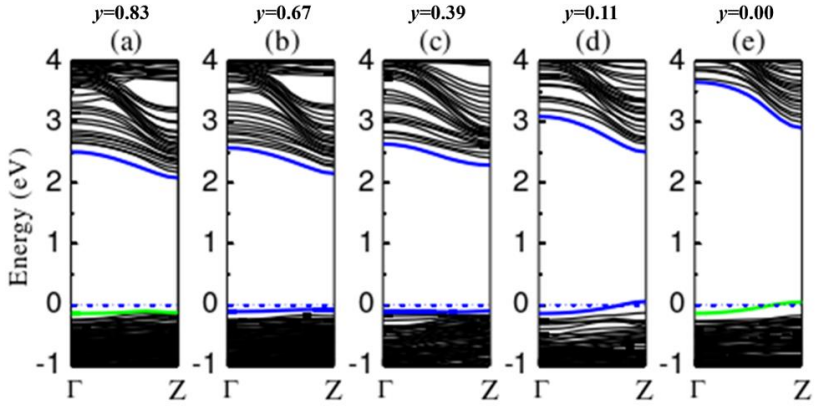

Fig.S13 Band structure diagrams of 2.88nm $MAPb_xSr_{1-x}(I_yCl_{1-y})_3$ core-shell nanowires with {100} crystal planes (x=50%) of different component ratios y. The blue band represents the first localized electronic state of the nanowires, while the green band represents the first extended electronic state of the nanowires (including surface electronic state and bulk electronic state).

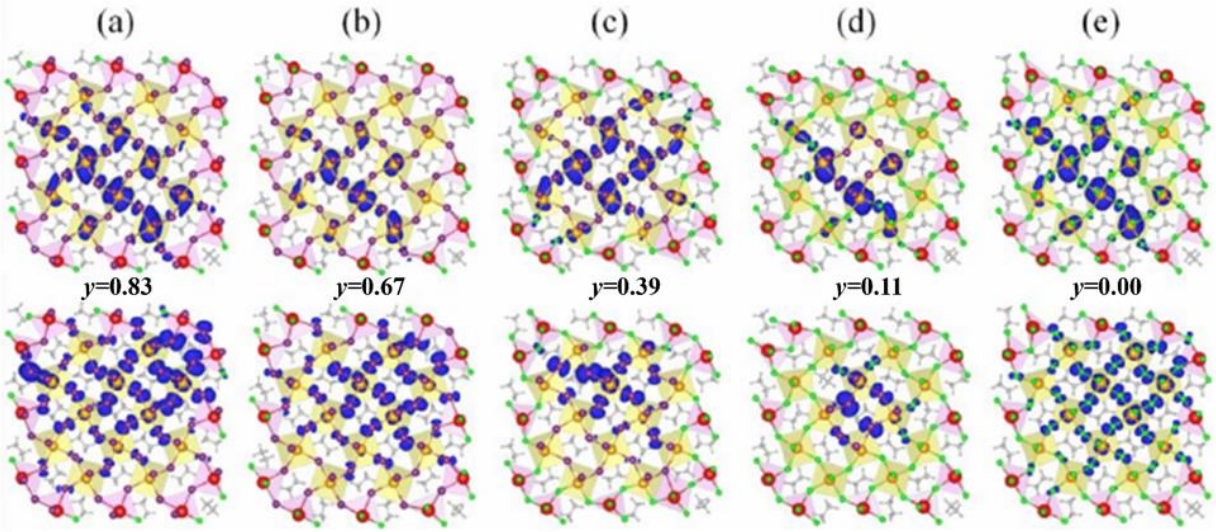

Fig.S14 Distribution of electronic states of the band edge of 2.88nm $MAPb_xSr_{1-x}(I_yCl_{1-y})_3$ core-shell nanowires (x=50%) with {100} crystal planes at different component ratios y.

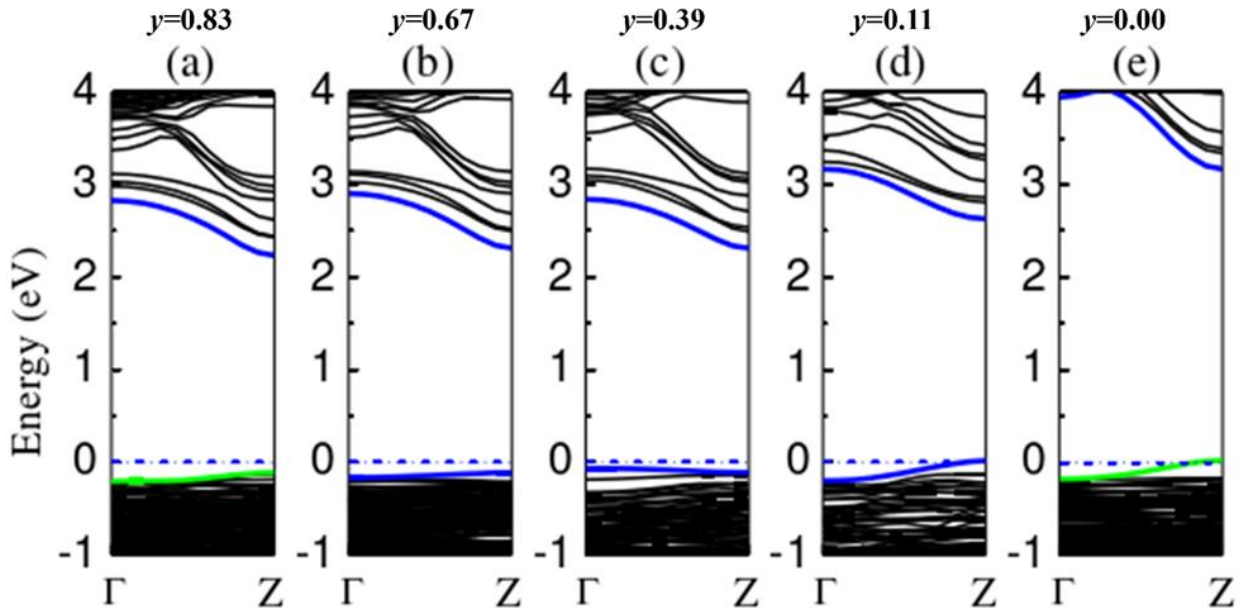

Fig.S15 Band structure diagrams of 2.88nm nm $MAPb_xSr_{1-x}I_yCl_{1-y}$ core-shell nanowires with {100} crystal planes (x=17%) of different component ratios y. The blue band represents the first localized electronic state of the nanowires, while the green band represents the first extended electronic state of the nanowires (including surface electronic state and bulk electronic state).

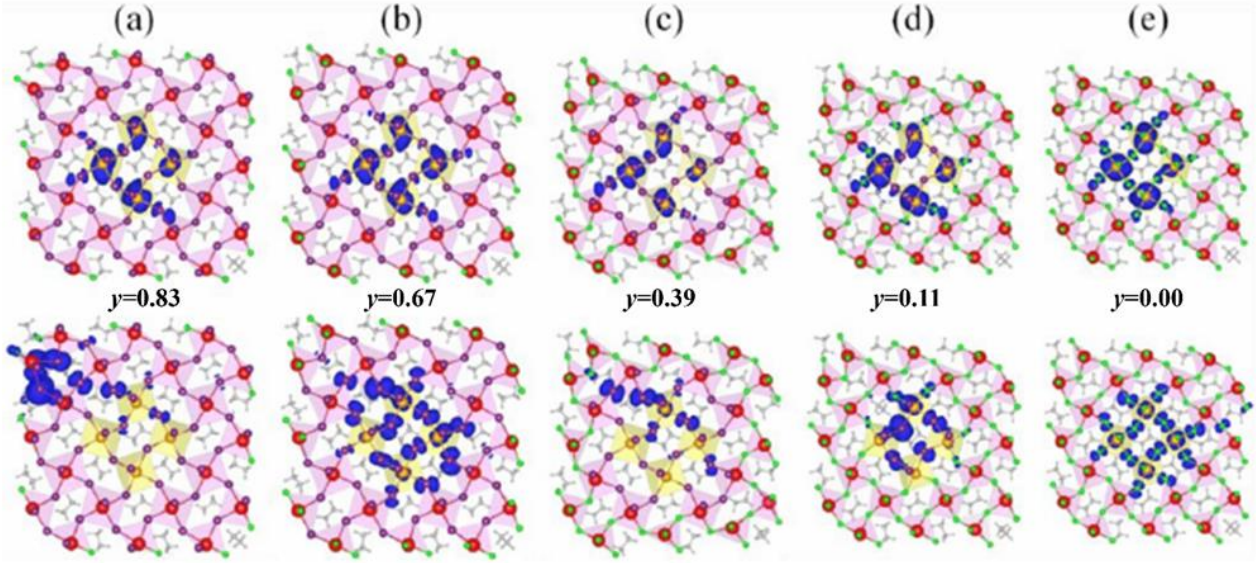

Fig.S16 The distribution of electronic states of the band edge of 2.88nm $MAPb_xSr_{1-x}(I_yCl_{1-y})_3$ core-shell nanowires (x=17%) with {100} crystal planes at different component ratios y.

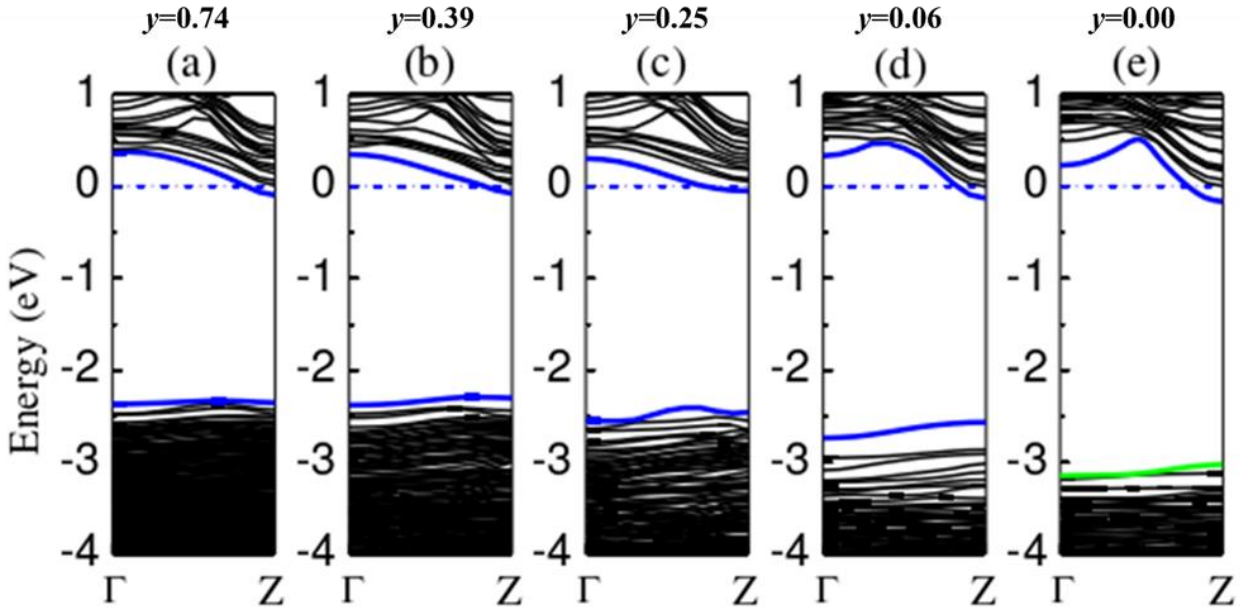

Fig.S17 Band structure diagrams of 3.08nm $MAPb_xSr_{1-x}(I_yCl_{1-y})_3$ core-shell nanowires with {110} crystal planes (x=56%) at different component ratios y. The blue band represents the first localized electronic state of the nanowires, while the green band represents the first extended electronic state of the nanowires (including surface electronic state and bulk electronic state).

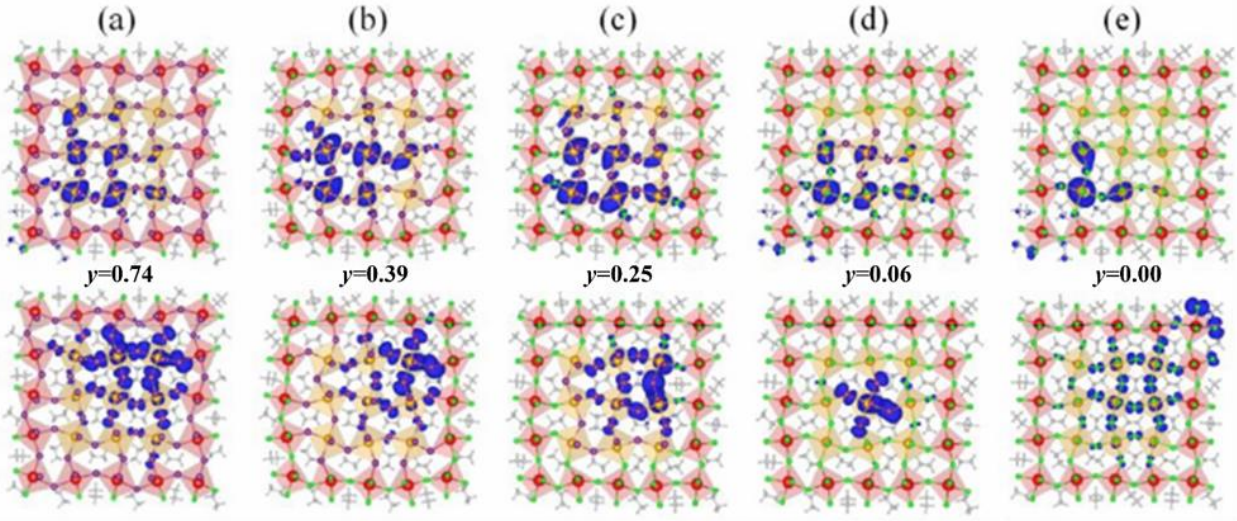

Fig.S18 The distribution of electronic states of the band edge of 3.08nm $MAPb_xSr_{1-x}(I_yCl_{1-y})_3$ core-shell nanowires (x=56%) with {110} crystal planes at different component ratios y.

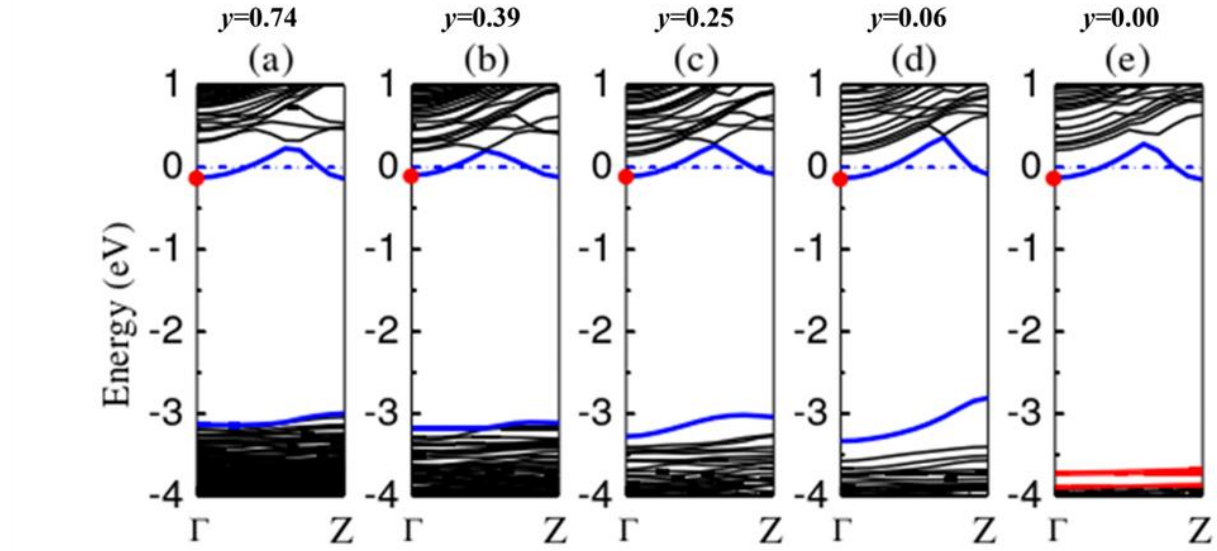

Fig.S19 Band structure diagrams of 3.08nm $MAPb_xSr_{1-x}(I_yCl_{1-y})_3$ core-shell nanowires with {110} crystal planes (x=4%) at different component ratios y. The blue band represents the first bulk localized electronic state of the nanowires, while the red band represents the surface electronic state of the nanowires.

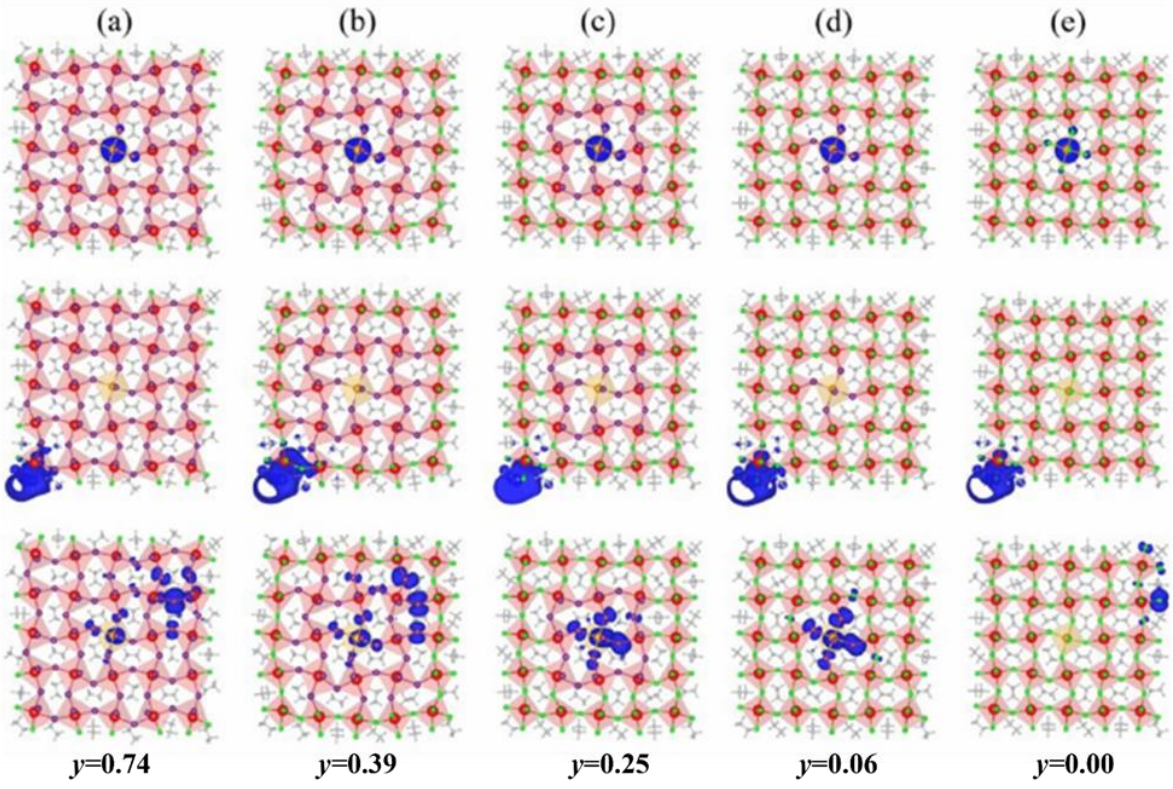

Fig.S20 Distribution of electronic states of the band edge of 3.08nm $MAPb_xSr_{1-x}(I_yCl_{1-y})_3$ core-shell nanowires (x=4%) with {110} crystal planes at different component ratios y: Excluding Γ point based CBM (top), the electronic states at Γ point of CBM (middle) and VBM (bottom).

Table.S3 The conduction band offset ($\Delta E_{C\text{-}I}$) and valence band offset ($\Delta E_{V\text{-}I}$) of $MAPb_xSr_{1-x}(I_yCl_{1-y})_3$ core-shell nanowires with different crystal planes and component ratios (x, y).

$MAPb_xSr_{1-x}(I_yCl_{1-y})_3$ Core-shell nanowire									
{100} crystal plane					{110} crystal plane				
	x=50%		x=16.67%			x=56.25%		x=4.00%	
I ratio y	$\Delta E_{C\text{-}I}$ (eV)	$\Delta E_{C\text{-}I}$ (eV)	$\Delta E_{C\text{-}I}$ (eV)	$\Delta E_{C\text{-}I}$ (eV)	I ratio y	$\Delta E_{C\text{-}I}$ (eV)	$\Delta E_{C\text{-}I}$ (eV)	$\Delta E_{C\text{-}I}$ (eV)	$\Delta E_{C\text{-}I}$ (eV)
83.33%	0.5508	0	0.6026	0	74.47%	0.4040	0.3584	0.4713	0.2795
66.67%	0.5465	0.1020	0.5936	0.1496	38.82%	0.4007	0.4849	0.3371	0.5003
38.89%	0.5395	0.1115	0.5699	0.2018	24.71%	0.3447	0.5407	0.2671	1.0136
11.11%	0.5007	0.2822	0.4063	0.2088	5.88%	0.2867	0.2963	0.254	0.7631
0%	0.2980	0	0	0	0%	0.1684	0	0.2113	0

The spatial distribution of holes in the valence band of the nanowires varies significantly under different component ratios (y). When y=0% or 100%, the holes will be distributed on the surface of the nanowire, while when $0<y<1$, the spatial distribution of holes is completely localized in the core region of the nanowire's bulk phase. This is because when $0<y<1$, both Cl and I elements exist in the nanowire. The stronger electronegativity of surface Cl element compared to internal I element shields the valence band holes at the center of the nanowire, resulting in a type-I band alignment. In addition, we have selected some typical $MAPb_xSr_{1-x}(I_yCl_{1-y})_3$ core-shell nanowires to specifically study their electronic structures and carrier spatial localization characteristics, as shown in **Fig.S21**. The electrons and holes of the $MAPb_xSr_{1-x}I_yCl_{1-y}$ core-shell nanowire are localized in the core region of the nanowires, forming type-I band alignment (**Fig.S21 e**). **Table.S3** presents the specific values of

the conduction and valence band offsets for all $MAPb_xSr_{1-x}(I_yCl_{1-y})_3$ core-shell nanowires.

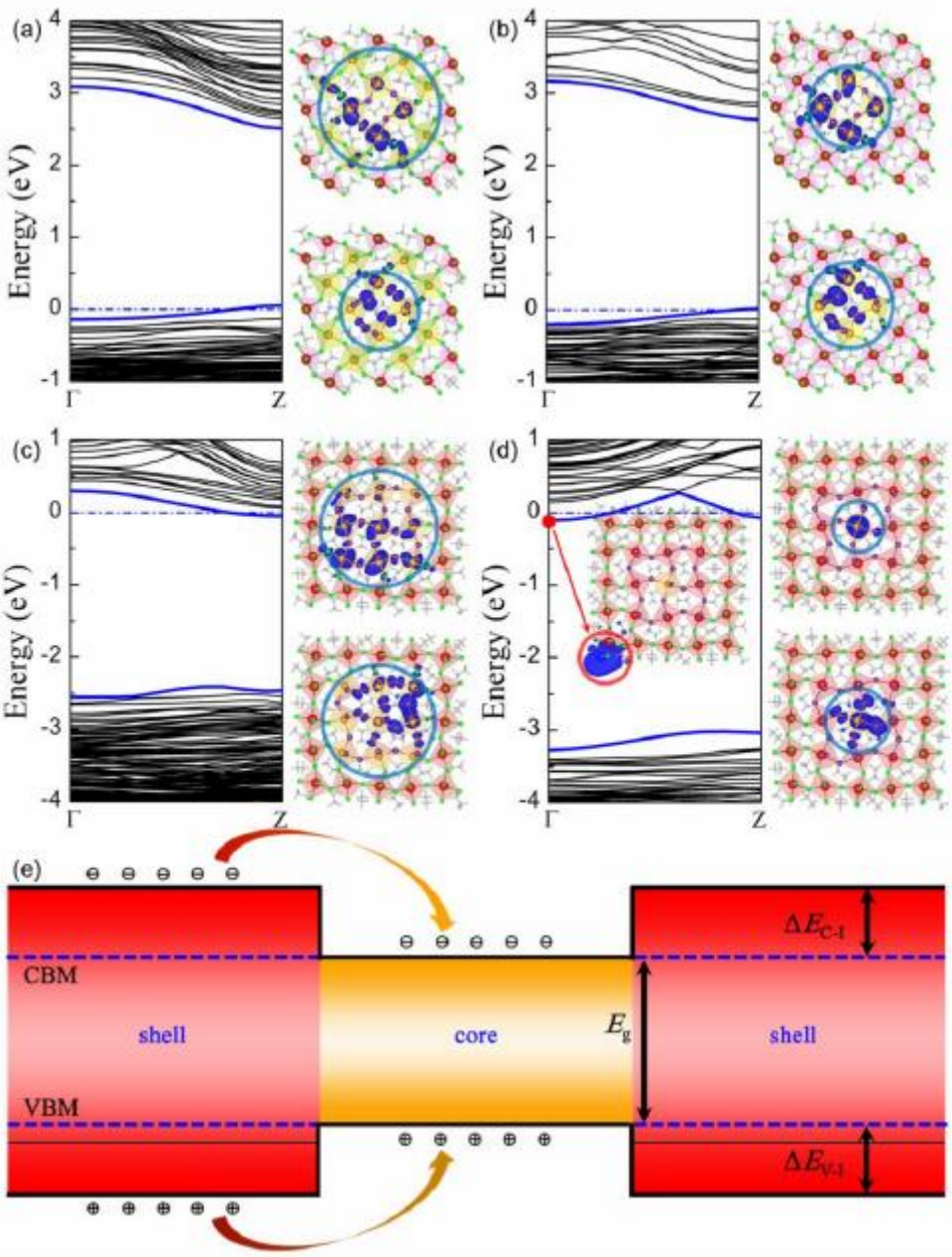

Fig.S21 The energy band structures (left) and charge densities of band edge (right) of nanowires with {100} crystal plane (a) x=0.50 and *y*=0.11, {100} crystal plane (b) *x*=0.17 and *y*=0.11, {110} crystal plane (c) *x*=0.56 and *y*=0.25, and {110} crystal plane (d) *x*=0.04 and *y*=0.25. (e) Schematic diagram of the band alignment of $MAPb_xSr_{1-x}(I_yCl_{1-y})_3$ core-shell nanowires. The circled charge density distribution corresponds to the energy bands marked in red, green, and blue. The position of the Fermi level is set to energy zero.

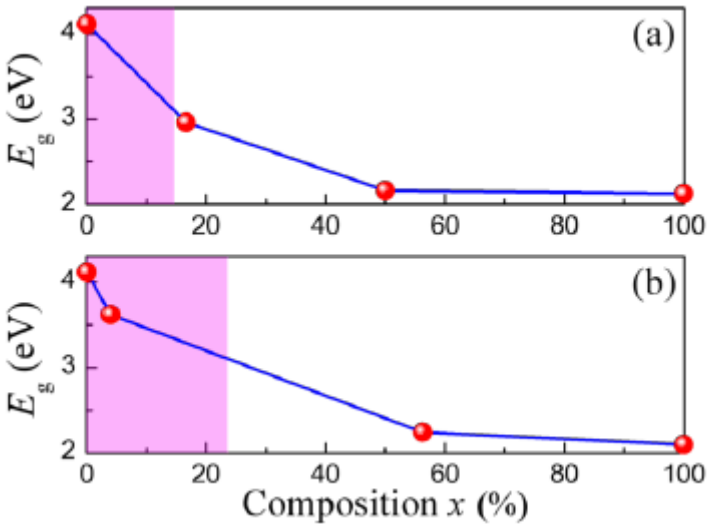

Fig.S22 (a) The band gaps of {100} and (b) {110} crystal plane core-shell nanowire varies with the composition x. The bandgap in the ultraviolet and visible light ranges is represented by purple shadows and white backgrounds, respectively.

REFERENCES

(1) Stoumpos C C, Malliakas C D, Kanatzidis M G. Semiconducting tin and lead iodide perovskites with organic cations: phase transitions, high mobilities, and near-infrared photoluminescent properties. *Inorg. Chem*. **2013**, 52, 9019-9038.

(2) Zhu X, Su H, Marcus R A, et al. Computed and experimental absorption spectra of the perovskite $CH_3NH_3PbI_3$. *J. Phys. Chem. Lett*. **2014**, 5, 3061-3065.

(3) Baikie T, Fang Y, Kadro J M, et al. Synthesis and crystal chemistry of the hybrid perovskite $(CH_3NH_3)PbI_3$ for solid-state sensitised solar cell applications. *J. Mater. Chem. A*. **2013**, 1, 5628-5641.

(4) Ding F, Dai J, Chen Y, et al. Broadband near-infrared metamaterial absorbers utilizing highly lossy metals. *Sci. Report*. **2016**, 6, 39445.

(5) Pazoki M, Jacobsson T J, Hagfeldt A, et al. Effect of metal cation replacement on the electronic structure of metalorganic halide perovskites: replacement of lead with alkaline-earth metals. *Phys. Rev. B*. **2016**, 93, 144105.

(6) Jacobsson T J, Pazoki M, Hagfeldt A, et al. Goldschmidt's rules and strontium replacement in lead halogen perovskite solar cells: theory and preliminary experiments on $CH_3NH_3SrI_3$. *J. Phys. Chem. C*. **2015**, 119, 25673-25683.

(7) Navas J, Sánchez-Coronilla A, Gallardo J J, et al. New insights into organic-inorganic hybrid

perovskite $CH_3NH_3PbI_3$ nanoparticles. An experimental and theoretical study of doping in Pb^{2+} sites with Sn^{2+}, Sr^{2+}, Cd^{2+} and Ca^{2+}. *Nanoscale*. **2015**, 7, 6216-6229.

(8) Uratani H, Yamashita K. Charge carrier trapping at surface defects of perovskite solar cell absorbers: a first-principles study. *J. Phys. Chem. Lett*. **2017**, 8, 742-746.

(9) Kumar A, Balasubramaniam K R, Kangsabanik J, et al. Crystal structure, stability, and optoelectronic properties of the organic-inorganic wide-band-gap perovskite $CH_3NH_3BaI_3$: candidate for transparent conductor applications. *Phys. Rev. B*. **2016**, 94, 180105.